arXiv:2206.01736v2 [eess.IV] 22 Jun 2022

Adaptive Adversarial Training to Improve Adversarial Robustness of DNNs for Medical Image Segmentation and Detection

Linhai Ma L.MA@MIAMI.EDU
Liang Liang LIANG@CS.MIAMI.EDU
Department of Computer Science
University of Miami, Coral Gables FL 33146, USA

Abstract

It is known that Deep Neural networks (DNNs) are vulnerable to adversarial attacks, and the adversarial robustness of DNNs could be improved by adding adversarial noises to training data (e.g., the standard adversarial training (SAT)). However, inappropriate noises added to training data may reduce a model's performance, which is termed the trade-off between accuracy and robustness. This problem has been sufficiently studied for the classification of whole images but has rarely been explored for image analysis tasks in the medical application domain, including image segmentation, landmark detection, and object detection tasks. In this study, we show that, for those medical image analysis tasks, the SAT method has a severe issue that limits its practical use: it generates a fixed and unified level of noise for all training samples for robust DNN training. A high noise level may lead to a large reduction in model performance and a low noise level may not be effective in improving robustness. To resolve this issue, we design an adaptive-margin adversarial training (AMAT) method that generates sample-wise adaptive adversarial noises for robust DNN training. In contrast to the existing, classification-oriented adversarial training methods, our AMAT method uses a loss-defined-margin strategy so that it can be applied to different tasks as long as the loss functions are well-defined. We successfully apply our AMAT method to state-of-the-art DNNs, using five publicly available datasets. The experimental results demonstrate that: (1) our AMAT method can be applied to the three seemingly different tasks in the medical image application domain; (2) AMAT outperforms the SAT method in adversarial robustness; (3) AMAT has a minimal reduction in prediction accuracy on clean data, compared with the SAT method; and (4) AMAT has almost the same training time cost as SAT. Please contact the authors for the source code.

Keywords: Adversarial Robustness; Medical Image Segmentation; Cephalometric Landmark Detection; Blood Cell Detection.

© L. Ma & L. Liang.

1. Introduction

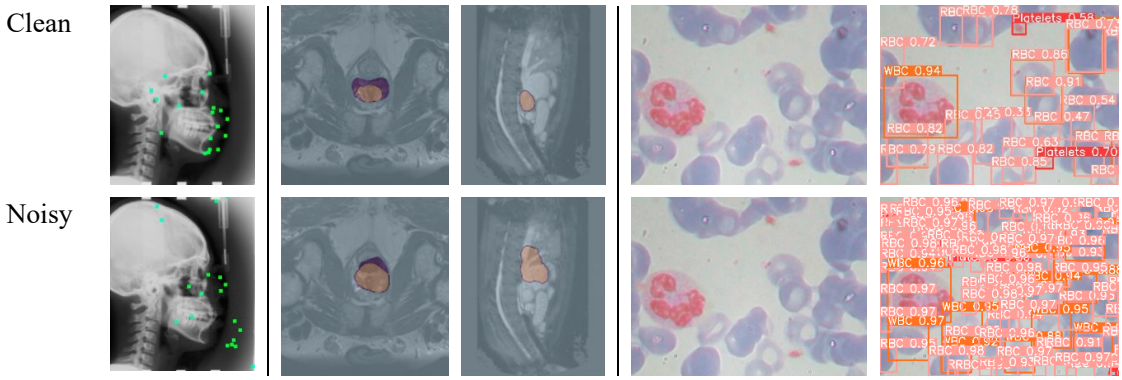


Figure 1: Examples of adversarial attacks against cephalometric landmark detection (a), segmentation of prostate (b) and heart (c), and blood cell detection ((d) is the input image and (e) is the detection result). By adding adversarial noises to the original/clean images (the first row), the noisy images are obatained (the second row). DNN outputs are significantly changed when the input images contain adversarial noises.

Recent methods based on Deep Neural Networks (DNNs) have achieved high accuracy for medical image analysis, including three basic tasks: segmentation, landmark detection, and object detection. However, DNNs are vulnerable to imperceptible adversarial noises Szegedy et al. (2014); Carlini and Wagner (2017); Brendel et al. (2018); Croce and Hein (2020); Joel et al. (2021); Moosavi-Dezfooli et al. (2016); Ozbulak et al. (2019); Madry et al. (2018); Paschali et al. (2018) (see Fig. 1), which makes it dangerous to deploy DNN-based decision-making systems for life-critical applications, such as medical image-based diagnosis. To make DNNs robust to adversarial noises, adding adversarial noises to training data (i.e., adversarial training) is an effective and general strategy Goodfellow et al. (2015); Madry et al. (2018). However, inappropriate noises added to training data may reduce a model's performance, which is termed the trade-off between accuracy and robustness. For the classification of whole images (e.g., the MNIST dataset), this problem has been sufficiently studied and a tremendous number of defense methods have been proposed to resolve this problem: TRADES Zhang et al. (2019) and MART Wang et al. (2020) optimize a loss with a KL divergence-based regularization term to make a trade-off between adversarial robustness and standard accuracy. DAT Wang et al. (2019) uses convergence quality as a criterion to adjust adversarial training perturbations. ATESSitawarin et al. (2020) and CAT Cai et al. (2018) apply curriculum strategy for adversarial training. IAATBalaji et al. (2019), FATZhang et al. (2020), Customized ATCheng et al. (2020), MMADing et al. (2020) and IMAMa and Liang (2020) are adaptive adversarial training methods and adjust the noise added to training data in the training process based on the classification-aware strategy. GAIRAT Zhang et al. (2021) applies sample-wise weights to the loss for robust training and the weights are related to the decision boundary.

As a comparison, for image segmentation, landmark detection, and object detection tasks in the medical image application domain, the trade-off between accuracy and robustness has rarely been explored and the number of defense methods Liu et al. (2020); He et al. (2019);

Daza et al. (2021) pales. Some of these defense methods are either not effective enough Uesato et al. (2018); Liu et al. (2020), or only work for very limited network structures He et al. (2019).

To improve adversarial robustness of DNNs for classification-related tasks, the standard adversarial training (SAT) method Goodfellow et al. (2015); Kurakin et al. (2017); Madry et al. (2018) is often considered Daza et al. (2021): given a fixed noise level ε (Lp vector norm), generate a noisy/adversarial sample $(\tilde{x}, y)$ using the PGD algorithm in Madry et al. (2018), where $\tilde{x} = PGD(x, y, \varepsilon)$ and $||x - \tilde{x}||_p \leq \varepsilon$; for every sample (x, y) in the training set; use the clean data $\{(x, y)\}$ and adversarial/noisy data $\{(\tilde{x}, y)\}$ together to train the model. The SAT loss function is given in Goodfellow et al. (2015):

$$L_{SAT} = (L(f(x), y) + L(f(\tilde{x}), y))/2 \tag{1}$$

where L is the original loss function for training the DNN model f. However, as will be shown in this study, the SAT method is problematic.

In our work to improve the adversarial robustness of DNNs for the three basic tasks (image segmentation, landmark detection, and object detection), we have made the following contributions. (1) We investigate the problem of SAT in the medical image segmentation, landmark detection, and object detection tasks: when the training noise level ε increases, the performance of SAT-trained models improves on data with larger noises, but drops on clean data or data with smaller noises, which indicates that a fixed and unified level of noise for training is inadequate. (2) To solve this problem, we design and implement an adaptive-margin adversarial training (AMAT) method for medical image segmentation, landmark detection, and object detection. AMAT generates sample-wise adaptive noises for robust DNN training, instead of using a fixed and unified noise level. In this way, the trained DNN model can have good resistance to adversarial noises while maintaining good accuracy on clean data. Furthermore, AMAT uses a loss-defined-margin strategy so that it can be applied to three different tasks of image segmentation, landmark detection, and object detection. (3) We successfully apply our AMAT method to improving adversarial robustness of three state-of-the-art DNNs for medical image segmentation, landmark detection, and object detection tasks. Five publicly available medical datasets are used for evaluation. The experimental results demonstrate that: (a) our AMAT method can be applied to the three fundamental tasks in the medical image application domain; (b) AMAT outperforms the SAT method in adversarial robustness on noisy data; (c) AMAT has a minimal reduction in prediction accuracy on clean data, compared with SAT; and (d) AMAT has almost the same training time cost as SAT.

2. Methodology

2.1. Adaptive Margin Adversarial Training (AMAT)

In our AMAT method, the concept of "margin" is borrowed from support-vector machine Cortes and Vapnik (1995), which means the distance between a data sample and the decision boundary of a classifier. To improve classifier robustness, during training, the generated noisy/adversarial sample should not cross the true decision boundary (i.e., $\tilde{x}$ and x have the same true label y). Since the clean samples have different distances to the true decision

Algorithm 1 Robust Training in One Epoch

Input:
S is the training set.
f is the DNN model.
$Loss$ is the loss function for training the model f.
Parameters:
$\mathcal{E}$ is the array of the estimated sample margins. $\mathcal{E}(i)$ is the margin of the sample indexed by the unique ID i. Every $\mathcal{E}(i)$ is initialized to be Δ_ε.
Δ_ε is the expansion step size (positive scalar).
ξ is threshold and it is determined by using the loss values on clean data (see Section 2.2).
Output: Updated model f after this training epoch.
Process:

1: **for** each training sample $(x,\ y)$ with ID i in S **do**
2: Run the model f on clean sample: $\hat{y} = f(x)$
3: Generate a noisy sample using the PGD algorithm: $\tilde{x} = PGD(x, y, \mathcal{E}(i))$
4: Run the model f on noisy sample: $\tilde{y} = f(\tilde{x})$
5: $L_0 = Loss(\hat{y},\ y)$
6: $L_1 = Loss(\tilde{y},\ y)$
7: $L = (L_0 + L_1)/2$
8: Back-propagate from L and update the model f
9: **if** $L_1 < \xi$ **then**
10: $\mathcal{E}(i) = \mathcal{E}(i) + \Delta_\varepsilon$ (Enlarge the margin)
11: **else**
12: $\mathcal{E}(i) = (||x - \tilde{x}||_p + \mathcal{E}(i))/2$ (Refine the margin)
13: **end if**
14: **end for**

Note: The algorithm runs in mini-batches. $||.||_p$ denotes vector Lp norm.

boundary, the noisy samples should contain different levels of noises. In this study, although the three tasks are not simple classification of whole images, the margin concept can be generalized: the "margin" of a sample x is defined as the maximum level of noise that can be added to the sample without harming the DNN performance on clean data. The basic idea of AMAT is to let each training sample have its own "margin", instead of using a fixed noise level as SAT.

The AMAT training process is shown in Algorithm 1, which includes two sub-processes: (1) compute the loss and update the DNN model (Line 2 to 8); and (2) update the sample margins (Line 9 to 12). x is the input (clean) image, $\hat{y}$ is the DNN output (e.g., segmentation map), and i is the unique ID for the clean sample $(x,\ y)$. Given the sample i and its estimated margin $\mathcal{E}(i)$, PGD Madry et al. (2018) is used to generate a noisy sample $\tilde{x}$ (Line 3). The model f runs on the clean and noisy samples to generate the outputs. Then, the loss L_0 on clean data and the loss L_1 on noisy data are calculated and combined. Finally, back-propagation runs to update the model. It is important not to add too much noise, because large noise may harm the DNN performance on clean data. To this end, we add the condition $L_1 < \xi$ to control the noise. Generally, the loss L_1 on the noisy sample will increase if the

noise level increases. In order to preserve DNN performance on clean data, the loss L_1 should not be significantly larger than the average loss value on clean data. We note that our novel strategy enables loss-defined-margin for each individual sample, and it also enables our AMAT method to handle different tasks as long as the loss functions are well-defined.

2.2. Value of ξ

The threshold ξ is used to determine if the noise is too large to be added on a sample for training. Assuming that on the clean training set $S = \{(x_i, y_i)|i = 1, 2, ...\}$, the DNN model f has been well trained; and $Loss$ is the loss function for training f on S. Then, we can obtain the loss values of all training samples, denoted by $V = \{Loss(f(x), y)|(x, y) \in S\}$. In our experiments, we observe that the distribution of the loss values approximately follows Normal distribution. The mean loss value $mean(V)$ and the standard deviation of the loss values $std(V)$ can be obtained. Then, the threshold ξ can be $mean(V)$ or $mean(V) + 2 \cdot std(V)$, and the choice is dependent on the dataset.

2.3. Loss function with multiple items

For some DNN models, the training loss function contains multiple loss terms. For instance, YOLO v5 Jocher et al. (2022) (used in Section 3.3) has three loss terms. If the loss function contains K loss terms, a small modification is made to Algorithm 1: (1) The threshold ξ becomes a vector of K scalars, and each scalar is calculated by using each of the K distributions of the loss terms on clean data; (2) Line 9 is modified to:

$$\textbf{if}(L_1[1] < \xi[1])\&(L_1[2] < \xi[2])\&...\&(L_1[K] < \xi[K])\textbf{then} \tag{2}$$

In short, all of the loss terms are considered separately. *mean* and *std* (see Section 2.2) are computed for each loss term. When all of the loss terms on noisy data are smaller than their corresponding thresholds, the noise is acceptable for training.

3. Experiment Configuration

3.1. Basic settings

All of the experiments are conducted on a server with Nvidia Tesla V100 GPU and Intel(R) Xeon(R) E5-2698 v4 CPU processor (2.20GHz). Three state-of-the-art DNN models and five publicly available medical image datasets are used for method evaluation: three for segmentation, one for landmark detection, and one for object detection.

3.2. Evaluated defense methods

In the experiments, the model trained only on clean data by the regular standard training method is named "STD"; the model trained by the SAT method with the noise level of ε is named "SATε"; the model trained by our AMAT method is called "AMAT". To our knowledge, there are no other adaptive adversarial training methods for image segmentation, landmark detection and object detection in medical image application domain. The SAT method is still most widely used in many applications. Except for SAT, the existing well-known adversarial training methods are designed for the classification of a whole image (e.g.,

MNIST digit images with the size of 28x28), and these methods cannot be applied to medical image segmentation, landmark detection, or object detection tasks in this study. Thus, we only use SAT with different ε as the baseline method in the experiments.

3.3. Method Evaluation

PGD-based adversarial attack is widely used for adversarial defense method evaluation Uesato et al. (2018); Tramer et al. (2020). The noises for evaluation are generated by PGD whitebox attack Madry et al. (2018) with 100 iterations (100-PGD). We also applied IFGSM whitebox attack Kurakin et al. (2018) with 10 iterations (10-IFGSM).The maximum attack noise level in the evaluation is selected such that the prediction accuracy drops to almost 0 (except for Landmark Detection).

3.4. L2 norm is used to measure noise level

It has been observed that adversarial noises have inner structures and patterns (see Fig. 1 in Goodfellow et al. (2015), Fig. 1 in Yao et al. (2020), Fig. 2 in Akhtar and Mian (2018)), which is completely ignored by L-inf norm. This means L-inf is not a good measure of adversarial noises. Thus, in this paper, the adversarial noises are measured in the L2 norm.

3.5. Evaluation on image segmentation

In this experiment, we apply SAT and AMAT to a self-configuring DNN, nnUnet Isensee et al. (2021). The nnUnet can automatically configure itself, including preprocessing, network architecture, training, and post-processing for the dataset. The inputs of nnUnet are 2D slices of 3D images. Some of the image slices have poor quality, and the nnUnet does not filter them out, which leads to a big $std(V)$ (see Section 2.2) in the training set. As a result, in this experiment, for AMAT, ξ is set to $mean(V)$ (see Section 2.2). The "Average Dice Index (ADI)" is used as the metric, whose formula is:

$$ADI = \frac{1}{n} \times \sum_{i=1}^{n} \frac{2 \times TP_i}{2 \times TP_i + FP_i + FN_i} \tag{3}$$

Here, n is the number of samples in the test set. For the sample i, TP_i is the number of pixels in true-positive area, FP_i is the number of pixels in false-positive area, and FN_i is the number of pixels in false-negative area. The metric used in the evaluation of the nnUnet Isensee et al. (2021) is renamed "Total voxel Dice Index (TVDI)" in this paper, and it does not equally weight the samples. TVDI is always higher than ADI. We note that TVDI results are in the Appendix, and some are in Table 4. We use this TVDI metric to show that the clean TVDI values of our results are similar to the results reported in the original nnUnet paper Isensee et al. (2021).

Three public datasets are used in this experiment. The Heart MRI dataset Simpson et al. (2019) has 20 labeled 3D images: 16 for training, 1 for validation and 3 for testing. The median shape of each 3D image is $115 \times 320 \times 320$, of which 115 is the number of slices. In this experiment, only 2D segmentation is considered, so the input of the model is one slice. The batch size (40), input image size (320×256) are self-configured by nnUnet for this data set. The model is trained for 50 epochs, where each epoch contains 50 iterations.

Other training settings are the same as those in Isensee et al. (2021). For SAT, we tried three different noise levels (5, 15, 25). The Hippocampus MRI dataset Simpson et al. (2019) has 260 labeled 3D images: 208 for training, 17 for validation and 35 for testing. The median shape of each 3D image is $36 \times 50 \times 35$, where 36 is the number of slices. The batch size (366), the input image size (56×40) and network structure are self-configured by nnUnet for this data set. The model is trained for 100 epochs, where each epoch has 50 iterations. Other training settings are the same as those in Isensee et al. (2021). For SAT, we tried four different noise levels (1, 5, 10, 15). The Prostate MRI dataset Simpson et al. (2019) has 32 labeled 3D images: 25 for training, 2 for validation and 5 for testing. The median shape of each 3D image is $20 \times 320 \times 319$, where 20 is the number of slices. The batch size (32), patch size (320×320) and network structure are self-configured by nnUnet for this dataset. The model is trained for 50 epochs, where each epoch has 50 iterations. Other training settings are the same as those in Isensee et al. (2021). For SAT, we tried three different noise levels (10, 20, 40).

3.6. Evaluation on landmark detection

In this experiment, we apply AMAT and SAT to the Multi-Task U-Net Yao et al. (2020). This model detects the landmarks by regressing both Gaussian heatmap and offset maps of the landmarks simultaneously. The loss function for this model has three loss terms, and therefore ξ is a vector of size 3, in which each value is set to $mean+2 \cdot std$ of the corresponding loss term values (Section 2.2). The original loss function contains a Binary Cross-Entropy (BCE) loss term. We find that, by replacing the BCE loss with Dice loss, the robustness of the Multi-Task U-Net becomes much better (Section 4). The Multi-Task U-Net trained with the original loss is denoted as "STD(BCE)", and the one trained with the Dice loss is denoted as "STD(Dice)". The two methods "SAT" and "AMAT" are applied to the "STD(Dice)" models. The metric for this experiment is "Mean Radial Error (MRE)" defined in Yao et al. (2020), which measures the Euclidean distance between true and predicted landmarks. MRE is scaled to the unit of mm. The dataset is created for cephalometric landmark detection in IEEE ISBI 2015 Challenge Wang et al. (2016). The dataset contains 400 cephalometric radiographs, which are officially split into 3 sets (Train, Test1, Test2): 150 for Train, 150 for Test1 and 100 for Test2. Because the performance of the models reported in Yao et al. (2020) is poor on Test2, we only use Test1. Test1 is further split into 2 sets: 50 for validation and 100 for testing. Each radiograph has 19 manually labeled landmarks of clinical anatomical significance by two expert doctors. The average annotations by two doctors is considered the ground truth. The images are resized to 200×160 in our experiment. The model is trained for 500 epochs. The batch size is 8. Other training settings are the same as those in Yao et al. (2020). For SAT, we tried three different noise levels (1, 3, 5).

3.7. Evaluation on object detection

In this experiment, we apply AMAT and SAT to the YOLO v5s object detector Jocher et al. (2022). The loss function has three loss terms, and therefore ξ is a vector of size 3, of which each value is set as $mean + 2 \cdot std$ of the corresponding loss term values (Section 2.2). The metric used for evaluation is mAP 0.5:0.95. The metric used for tuning the hyperparameter is Average Intersection over Union (IOU) of all detected objects (Section 3.8). The dataset

is named BCCD, which is a small-scale dataset for blood cell detection Shenggan (2017). The dataset has 364 2D images, which is split into 3 sets: 294 for training, 33 for validation and 37 for testing. The blood cells on each image are from three classes: Red Blood Cell, White Blood Cell, and Platelets. Each image is resized to 320×320 in our experiment. The model is trained for 300 epochs. The batch size is 32. Other training settings are the same as Jocher et al. (2022). For SAT, we tried three different noise levels (1, 10, 15).

3.8. Selection of step size Δ_ε

AMAT has the hyperparameter, Δ_ε, that needs to be tuned, and a grid search on the validation set can be conducted to decide the best value. The metric for hyperparameter selection is AUC_{robust}, borrowed from Ma and Liang (2022):

$$AUC_{robust} = \sqrt{ACC_{clean} \times AUC_{||\tilde{x}-x||_p \leq \epsilon_{max}}} \tag{4}$$

where ACC_{clean} is the model accuracy on clean data (i.e., dice score for image segmentation, MRE for landmark detection, and IOU for object detection). $AUC_{||\tilde{x}-x||_p \leq \epsilon_{max}}$ is the normalized area under the curve of accuracy vs. noise level, which is the average accuracy across a range of noise levels, i.e.$||\tilde{x} - x||_p \leq \epsilon_{max}$. Here, ϵ_{max} is the max noise level of the adversarial attack. $\tilde{x}$ and x are defined in Algorithm 1. Therefore, AUC_{robust} is the overall performance measure that takes both accuracy on clean data and robustness into consideration. The detailed grid search results are shown in the Appendix A. The configurations are the same as that mentioned in Section 3. Appendix A shows that the performance of AMAT is not significantly sensitive to the choice of Δ_ε, except too small Δ_ε. This is because AMAT with too small Δ_ε may need more training epochs to converge, while the grid research has a fixed number of epochs for each run.

From Table 8, 9, 10, 11, 12 in Appendix A, the optimal Δ_ε of AMAT for the experiments, Heart, Hippocampus, Prostate, Cephalometric and BCCD are 5, 0.5, 3, 1 and 3.5.

4. Results and Discussions

4.1. Segmentation results on the three datasets (Heart, Hippocampus, and Prostate:

Table 1: ADI of nnUnet on Heart test set: "S. Dice" denotes the ADI on clean data; "P. ϵ" denotes PGD attack with noise level ϵ; "IF. ϵ" denotes IFGSM attack with noise level ϵ; "Avg." denotes average performance on noisy data

Methods	S. Dice	P. 5	P. 10	P. 15	Avg.	IF. 5	IF. 10	IF. 15	Avg.
AMAT	**0.9148**	0.8476	0.7594	0.6588	**0.7553**	0.8834	0.8532	0.8255	**0.8540**
PGD25	0.6652	0.6175	0.5711	0.5355	0.5747	0.6410	0.6173	0.6017	0.6200
PGD15	0.7188	0.6579	0.5869	0.5194	0.5881	0.6933	0.6640	0.6329	0.6634
PGD5	0.7525	0.6565	0.5542	0.4617	0.5575	0.7087	0.6667	0.6370	0.6708
STD	0.7954	0.5197	0.1997	0.0172	0.2455	0.6930	0.6238	0.5779	0.6316

Table 2: ADI of nnUnet on Hippocampus test set: "S. Dice" denotes the ADI on clean data; "P. ϵ" denotes PGD attack with noise level ϵ; "IF. ϵ" denotes IFGSM attack with noise level ϵ; "Avg." denotes average performance on noisy data

Methods	S. Dice	P. 2	P. 6	P. 10	Avg.	IF. 2	IF. 6	IF. 10	Avg.
AMAT	**0.7845**	0.7525	0.6752	0.5580	**0.6619**	0.7587	0.7280	0.6968	**0.7278**
PGD15	0.7112	0.6762	0.5938	0.4833	0.5844	0.6891	0.6600	0.6276	0.6589
PGD10	0.7175	0.6768	0.5953	0.4707	0.5809	0.6949	0.6599	0.6232	0.6593
PGD5	0.7305	0.6866	0.5636	0.4213	0.5572	0.7013	0.6580	0.6195	0.6596
PGD1	0.7510	0.6616	0.4192	0.1752	0.4187	0.7067	0.6303	0.5693	0.6354
STD	0.7589	0.5217	0.0379	0.0015	0.1870	0.6572	0.5105	0.3870	0.5182

Table 3: ADI of nnUnet on Prostate test set: "S. Dice" denotes the ADI on clean data; "P. ϵ" denotes PGD attack with noise level ϵ; "IF. ϵ" denotes IFGSM attack with noise level ϵ; "Avg." denotes average performance on noisy data

Methods	S. Dice	P. 10	P. 20	P. 40	Avg.	IF. 10	IF. 20	IF. 40	Avg.
AMAT	**0.8336**	0.7991	0.7572	0.6528	**0.7364**	0.8180	0.8014	0.7649	**0.7948**
PGD40	0.6152	0.5423	0.4614	0.3085	0.4374	0.5817	0.5453	0.4768	0.5346
PGD20	0.6640	0.5606	0.4510	0.2779	0.4298	0.6181	0.5698	0.4772	0.5550
PGD10	0.6569	0.5405	0.4034	0.2063	0.3834	0.5981	0.5522	0.4676	0.5393
STD	0.7418	0.3012	0.1428	0.0455	0.1632	0.5252	0.4138	0.2796	0.4062

From Table 4, the TVDI values of three "STD" models are similar to those in Isensee et al. (2021), which indicates that the number of training epochs is enough for the models to converge. From Table 1, Table 2 and Table 3, we have the following observations. (1) AMAT has the best performance: the "AMAT" models have the highest average ADI on noisy data; the "AMAT" model has the highest ADI on clean data, even higher than the "STD" model. (2) Under the 100-PGD attack, the ADI of the "STD" models drops to almost 0 on the noise level 15 on the Heart dataset, on the noise level 10 on the Hippocampus dataset, and on the noise level 40 on the Prostate dataset. (3) The "$SAT\varepsilon$" models with smaller ε have better performance on lower-noise data, but worse performance on higher-noise data. (4) The "$SAT\varepsilon$" models with larger ε have better performance on higher-noise data, but worse performance on lower-noise data and clean data.

Table 4: TDVI of "STD" models on three datasets

Task	TVDI
Heart	0.92
Hippocampus	0.88
Prostate	0.82

Table 5: Time cost for each training epoch (Seconds): Columns 1-3 are for segmentation; Column 4 is for landmark detection; Column 5 is for blood cell detection.

-	Heart	Hippocampus	Prostate	Landmark	BCCD
STD	31	10	20	12	6
SAT	476	114	465	50	30
AMAT	480	120	467	53	35

4.2. Landmark detection results on the Cephalometric dataset

Table 6: MRE (mm) of Multi-Task Unet on Cephalometric test set: "MRE" denotes the MRE on clean data; "P. ϵ" denotes PGD attack with noise level ϵ; "IF. ϵ" denotes IFGSM attack with noise level ϵ; "Avg." denotes average performance on noisy data. MRE is the lower the better.

Methods	MRE	P. 0.5	P. 1	P. 2	Avg.	IF. 0.5	IF. 1	IF. 2	Avg.
AMAT	**1.773**	1.891	2.044	2.415	**2.117**	1.892	2.037	2.391	**2.107**
SAT1	1.814	1.948	2.057	2.457	2.154	1.948	2.060	2.427	2.145
SAT3	2.108	2.187	2.270	2.477	2.311	2.187	2.274	2.469	2.310
SAT5	2.177	2.263	2.342	2.543	2.383	2.264	2.343	2.545	2.384
STD(BCE)	1.545	4.345	14.295	38.868	19.169	3.929	10.910	35.015	16.618
STD(Dice)	1.623	3.378	8.289	32.820	14.829	3.077	6.245	21.285	10.202

From Table 6, observations are as follows. (1) AMAT has the best performance: The "AMAT" model has the smallest Avg. MRE on noisy data; The "AMAT" model has the smallest Avg. MRE on clean data among all defense methods. (2) The "STD(Dice)" model is better than the "STD(BCE)" model. But both of them are very vulnerable to 100-PGD and 10-IFGSM adversarial attacks. (3) The "$SAT\varepsilon$" models with smaller ε have better performance on lower-noise data and clean data, but not as good as AMAT. (4) The "$SAT\varepsilon$" models with larger ε have worse performance on lower-noise data and clean data.

4.3. Blood cell detection results on the BCCD dataset

Table 7: mAP0.5:0.95 of YOLO V5 on BCCD test set: "mAP" denotes the mAP0.5:0.95 on clean data; "P. ϵ" denotes PGD with noise level ϵ; "IF. ϵ" denotes IFGSM attack with noise level ϵ; "Avg." denotes average performance on noisy data

Methods	mAP	P. 5	P. 10	P. 15	Avg.	IF. 5	IF. 10	IF. 15	Avg.
AMAT	**0.5989**	0.3341	0.2017	0.1428	**0.2262**	0.3350	0.2106	0.1511	**0.2322**
SAT1	0.5810	0.2845	0.1467	0.0815	0.1709	0.2954	0.1762	0.1228	0.1981
SAT10	0.4722	0.2988	0.1869	0.0765	0.1874	0.2988	0.1868	0.0808	0.1888
SAT15	0.2565	0.2013	0.1375	0.0572	0.1320	0.2015	0.1354	0.0603	0.1324
STD	0.5993	0.0072	0.0007	0.0005	0.0028	0.0456	0.0102	0.0082	0.0213

From Table 7, observations are as follows. (1) AMAT has the best performance: The "AMAT" model has the best average performance on noisy data; The "AMAT" model has the best performance on clean data among all defense methods, very close to "STD". (2) The performance of the "STD" model drops to 0 on very small noise levels. (3) "$SAT\varepsilon$" models with smaller ε has better performance on lower-noise data and clean data, but not as good as AMAT. (4)"$SAT\varepsilon$" models with larger ε has worse performance on lower-noise data and clean data.

4.4. Discussion

We have those observations from the experiments. (1) Our AMAT method has the best performance: AMAT has the best average performance on noisy data, compared to STD

and SAT; AMAT has better performance on clean data, compare to SAT. In the image segmentation of Heart, Hippocampus and Prostate, AMAT even outperforms STD on clean data. This suggests that properly crafted adversarial training noise may not have to harm the model's performance. In other words, the trade-off between accuracy and robustness can be lifted for this task: we do not need to sacrifice accuracy (on clean data) in exchange for robustness. This is also corroborated by a similar observation in a whole-image classification task Zhang et al. (2021). (2) Table 5 shows that AMAT has almost the same training time cost as SAT. (3) The noises measured by L2 norm in the experiments are very small on each pixel, but the performance of the "STD" models drops to almost zero on small noise levels, which indicates the 100-PGD is a very strong and covert threat to segmentation and detection tasks. (4) The "$SAT\varepsilon$" models with larger ε have worse performance on lower-noise data, and the "$SAT\varepsilon$" models with smaller ε have poor performance on higher-noise data. This indicates that a fixed and unified level of noise is inadequate for robust DNN training. For life-critical medical image analysis applications, the DNN models should have a good performance on both clean data and noisy data. Thus, "AMAT" with adaptive training noises is more suitable than "SATε" with a fixed and unified noise level ε.

5. Conclusion

We propose an adaptive adversarial training method, AMAT, to make DNNs robust against adversarial attacks/noises in medical image segmentation, landmark detection, and object detection tasks, and the key idea is to adaptively adjust the training noises for individual training samples, so that the trained DNN model will have good resistance to the adversarial noises while maintaining good accuracy on clean data. We apply our proposed method to three state-of-the-art DNNs on five publicly available medical image datasets. The experiment results show that our AMAT method outperforms the SAT method in both adversarial robustness and prediction accuracy on clean data, while having almost the same training time cost as SAT. We hope our approach may facilitate the development of robust DNNs for more medical applications in the future.

References

Naveed Akhtar and Ajmal Mian. Threat of adversarial attacks on deep learning in computer vision: A survey. *IEEE Access*, 6:14410–14430, 2018.

Yogesh Balaji, Tom Goldstein, and Judy Hoffman. Instance adaptive adversarial training: Improved accuracy tradeoffs in neural nets. *arXiv preprint arXiv:1910.08051*, 2019.

Wieland Brendel, Jonas Rauber, and Matthias Bethge. Decision-based adversarial attacks: Reliable attacks against black-box machine learning models. In *ICLR*, 2018.

Qi-Zhi Cai, Chang Liu, and Dawn Song. Curriculum adversarial training. In *Proceedings of the 27th International Joint Conference on Artificial Intelligence*, pages 3740–3747, 2018.

Nicholas Carlini and David Wagner. Towards evaluating the robustness of neural networks. In *2017 ieee symposium on security and privacy (sp)*, pages 39–57. IEEE, 2017.

Minhao Cheng, Qi Lei, Pin-Yu Chen, Inderjit Dhillon, and Cho-Jui Hsieh. Cat: Customized adversarial training for improved robustness. *arXiv preprint arXiv:2002.06789*, 2020.

Corinna Cortes and Vladimir Vapnik. Support-vector networks. *Machine learning*, 20(3): 273–297, 1995.

Francesco Croce and Matthias Hein. Reliable evaluation of adversarial robustness with an ensemble of diverse parameter-free attacks. In *International conference on machine learning*, pages 2206–2216. PMLR, 2020.

Laura Daza, Juan C Pérez, and Pablo Arbeláez. Towards robust general medical image segmentation. In *International Conference on Medical Image Computing and Computer-Assisted Intervention*, pages 3–13. Springer, 2021.

Gavin Weiguang Ding, Yash Sharma, Kry Yik Chau Lui, and Ruitong Huang. Mma training: Direct input space margin maximization through adversarial training. In *International Conference on Learning Representations*, 2020.

Ian Goodfellow, Jonathon Shlens, and Christian Szegedy. Explaining and harnessing adversarial examples. In *ICLR*, 2015.

Xiang He, Sibei Yang, Guanbin Li, Haofeng Li, Huiyou Chang, and Yizhou Yu. Non-local context encoder: Robust biomedical image segmentation against adversarial attacks. In *Proceedings of the AAAI Conference on Artificial Intelligence*, volume 33, pages 8417–8424, 2019.

Fabian Isensee, Paul F Jaeger, Simon AA Kohl, Jens Petersen, and Klaus H Maier-Hein. nnu-net: a self-configuring method for deep learning-based biomedical image segmentation. *Nature methods*, 18(2):203–211, 2021.

Glenn Jocher, Ayush Chaurasia, et al. ultralytics/yolov5: v6.1 - TensorRT, TensorFlow Edge TPU and OpenVINO Export and Inference, February 2022. URL https://doi.org/10.5281/zenodo.6222936.

Marina Z Joel, Sachin Umrao, Enoch Chang, Rachel Choi, Daniel Yang, James Duncan, Antonio Omuro, Roy Herbst, Harlan Krumholz, Sanjay Aneja, et al. Adversarial attack vulnerability of deep learning models for oncologic images. *medRxiv*, pages 2021–01, 2021.

Alexey Kurakin, Ian Goodfellow, and Samy Bengio. Adversarial machine learning at scale. In *ICLR*, 2017.

Alexey Kurakin, Ian J Goodfellow, and Samy Bengio. Adversarial examples in the physical world. In *Artificial intelligence safety and security*, pages 99–112. Chapman and Hall/CRC, 2018.

Qi Liu, Han Jiang, Tao Liu, Zihao Liu, Sicheng Li, Wujie Wen, and Yiyu Shi. Defending deep learning-based biomedical image segmentation from adversarial attacks: a low-cost frequency refinement approach. In *International Conference on Medical Image Computing and Computer-Assisted Intervention*, pages 342–351. Springer, 2020.

Linhai Ma and Liang Liang. Increasing-margin adversarial (ima) training to improve adversarial robustness of neural networks. *arXiv preprint arXiv:2005.09147*, 2020.

Linhai Ma and Liang Liang. A regularization method to improve adversarial robustness of neural networks for ecg signal classification. *Computers in Biology and Medicine*, 144: 105345, 2022.

Aleksander Madry, Aleksandar Makelov, Ludwig Schmidt, Dimitris Tsipras, and Adrian Vladu. Towards deep learning models resistant to adversarial attacks. In *ICLR*, 2018.

Seyed-Mohsen Moosavi-Dezfooli, Alhussein Fawzi, and Pascal Frossard. Deepfool: a simple and accurate method to fool deep neural networks. In *Proceedings of the IEEE conference on computer vision and pattern recognition*, pages 2574–2582, 2016.

Utku Ozbulak, Arnout Van Messem, and Wesley De Neve. Impact of adversarial examples on deep learning models for biomedical image segmentation. In *International Conference on Medical Image Computing and Computer-Assisted Intervention*, pages 300–308. Springer, 2019.

Magdalini Paschali, Sailesh Conjeti, Fernando Navarro, and Nassir Navab. Generalizability vs. robustness: investigating medical imaging networks using adversarial examples. In *International Conference on Medical Image Computing and Computer-Assisted Intervention*, pages 493–501. Springer, 2018.

Shenggan. Bccd dataset, 2017. URL https://github.com/Shenggan/BCCDDataset.

Amber L Simpson, Michela Antonelli, Spyridon Bakas, Michel Bilello, Keyvan Farahani, Bram Van Ginneken, Annette Kopp-Schneider, Bennett A Landman, Geert Litjens, Bjoern Menze, et al. A large annotated medical image dataset for the development and evaluation of segmentation algorithms. *arXiv preprint arXiv:1902.09063*, 2019.

Chawin Sitawarin, Supriyo Chakraborty, and David Wagner. Improving adversarial robustness through progressive hardening. 2020.

Christian Szegedy, Wojciech Zaremba, Ilya Sutskever, Joan Bruna, Dumitru Erhan, Ian Goodfellow, and Rob Fergus. Intriguing properties of neural networks. In *ICLR*, 2014.

Florian Tramer, Nicholas Carlini, Wieland Brendel, and Aleksander Madry. On adaptive attacks to adversarial example defenses. *Advances in Neural Information Processing Systems*, 33:1633–1645, 2020.

Jonathan Uesato, Brendan O'donoghue, Pushmeet Kohli, and Aaron Oord. Adversarial risk and the dangers of evaluating against weak attacks. In *International Conference on Machine Learning*, pages 5025–5034. PMLR, 2018.

Ching-Wei Wang, Cheng-Ta Huang, Jia-Hong Lee, Chung-Hsing Li, Sheng-Wei Chang, Ming-Jhih Siao, Tat-Ming Lai, Bulat Ibragimov, Tomaž Vrtovec, Olaf Ronneberger, et al. A benchmark for comparison of dental radiography analysis algorithms. *Medical image analysis*, 31:63–76, 2016.

Yisen Wang, Xingjun Ma, James Bailey, Jinfeng Yi, Bowen Zhou, and Quanquan Gu. On the convergence and robustness of adversarial training. In *International Conference on Machine Learning*, pages 6586–6595. PMLR, 2019.

Yisen Wang, Difan Zou, Jinfeng Yi, James Bailey, Xingjun Ma, and Quanquan Gu. Improving adversarial robustness requires revisiting misclassified examples. In *ICLR*, 2020.

Qingsong Yao, Zecheng He, Hu Han, and S Kevin Zhou. Miss the point: targeted adversarial attack on multiple landmark detection. In *International Conference on Medical Image Computing and Computer-Assisted Intervention*, pages 692–702. Springer, 2020.

Hongyang Zhang, Yaodong Yu, Jiantao Jiao, Eric Xing, Laurent El Ghaoui, and Michael Jordan. Theoretically principled trade-off between robustness and accuracy. In *International conference on machine learning*, pages 7472–7482. PMLR, 2019.

Jingfeng Zhang, Xilie Xu, Bo Han, Gang Niu, Lizhen Cui, Masashi Sugiyama, and Mohan Kankanhalli. Attacks which do not kill training make adversarial learning stronger. In *International conference on machine learning*, pages 11278–11287. PMLR, 2020.

Jingfeng Zhang, Jianing Zhu, Gang Niu, Bo Han, Masashi Sugiyama, and Mohan S Kankanhalli. Geometry-aware instance-reweighted adversarial training. In *ICLR*, 2021.

Appendix A. Selection of Δ_ε

Table 8: ADI of nnUnet on Heart validation set

Noise level	0	5	10	15	AUC_{Robust}
$\Delta_\varepsilon = 1$	0.8902	0.8373	0.7702	0.6930	0.8438
$\Delta_\varepsilon = 3$	0.9067	0.8520	0.7965	0.7363	0.8640
$\Delta_\varepsilon = 5$	0.9101	0.8673	0.8205	0.7681	**0.8755**
$\Delta_\varepsilon = 7$	0.9076	0.8657	0.8193	0.7757	0.8743
$\Delta_\varepsilon = 9$	0.9037	0.8608	0.8181	0.7675	0.8703

Table 9: ADI of nnUnet on Hippocampus validation set

Noise level	0	2	6	10	AUC_{Robust}
$\Delta_\varepsilon = 0.1$	0.7860	0.7460	0.6482	0.5004	0.7212
$\Delta_\varepsilon = 0.3$	0.7733	0.7418	0.6655	0.5562	0.7237
$\Delta_\varepsilon = 0.5$	0.7753	0.7407	0.6709	0.5590	**0.7260**
$\Delta_\varepsilon = 0.7$	0.7718	0.7408	0.6692	0.5522	0.7231
$\Delta_\varepsilon = 0.9$	0.7665	0.7374	0.6650	0.5640	0.7202
$\Delta_\varepsilon = 1.1$	0.7685	0.7373	0.6681	0.5583	0.7213
$\Delta_\varepsilon = 1.3$	0.7668	0.7371	0.6678	0.5663	0.7211
$\Delta_\varepsilon = 1.5$	0.7679	0.7364	0.6643	0.5640	0.7206

Table 10: ADI of nnUnet on Prostate validation set

Noise level	0	10	20	40	AUC_{Robust}
$\Delta_\varepsilon = 1$	0.8351	0.7981	0.7520	0.6339	0.7884
$\Delta_\varepsilon = 3$	0.8271	0.7972	0.7572	0.6637	**0.7890**
$\Delta_\varepsilon = 5$	0.8018	0.7756	0.7446	0.6757	0.7715
$\Delta_\varepsilon = 7$	0.8119	0.7872	0.7550	0.6774	0.7807
$\Delta_\varepsilon = 9$	0.8096	0.7835	0.7487	0.6731	0.7772
$\Delta_\varepsilon = 11$	0.8033	0.7781	0.7481	0.6762	0.7734

Table 11: MRE (mm) of Multi-Task Unet on Cephalometric validation set

Noise level	0	0.5	1	2	AUC_{Robust}
Δ_ε =0.1	1.637	1.906	2.247	3.870	0.5218
Δ_ε =0.5	1.735	1.918	2.103	2.817	0.5036
Δ_ε =1.0	1.773	1.892	2.044	2.426	**0.4947**
Δ_ε =1.5	1.893	1.992	2.117	2.388	0.5183
Δ_ε =2.0	1.978	2.081	2.195	2.420	0.5385

Table 12: Avg. IOU of YOLO V5 on BCCD validation set

Noise level	0	5	10	15	AUC_{Robust}
Δ_ε =0.5	0.7672	0.5444	0.3509	0.2640	0.6007
Δ_ε =1.0	0.7633	0.5539	0.3570	0.2718	0.6029
Δ_ε =1.5	0.7650	0.5657	0.3599	0.2697	0.6066
Δ_ε =2.0	0.7636	0.5683	0.3546	0.2718	0.6055
Δ_ε =2.5	0.7777	0.5720	0.3699	0.2601	0.6154
Δ_ε =3.0	0.7767	0.5775	0.3577	0.2686	0.6144
Δ_ε =3.5	0.7796	0.5776	0.3655	0.2792	**0.6186**
Δ_ε =4.0	0.7779	0.5733	0.3460	0.2632	0.6110
Δ_ε =4.5	0.7745	0.5501	0.3349	0.2573	0.6014
Δ_ε =5.0	0.7717	0.5572	0.3329	0.2319	0.5984

Appendix B. Formulars

$$TVDI = \frac{2 \times \sum_i^n TP_i}{2 \times \sum_i^n TP_i + \sum_i^n FP_i + \sum_i^n FN_i} \tag{5}$$

The notations are the same as equation (2) in Section 3.1.

Appendix C. Image samples

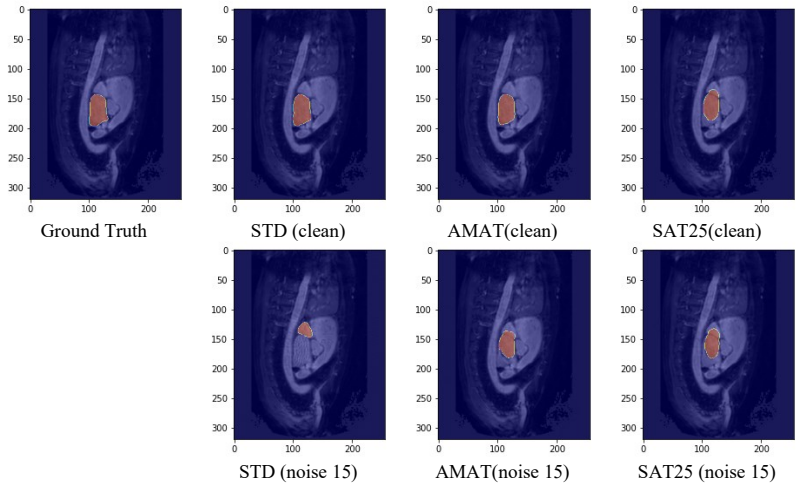


Figure 2: Examples of adversarial attacks against Heart MRI dataset (L2 norm)

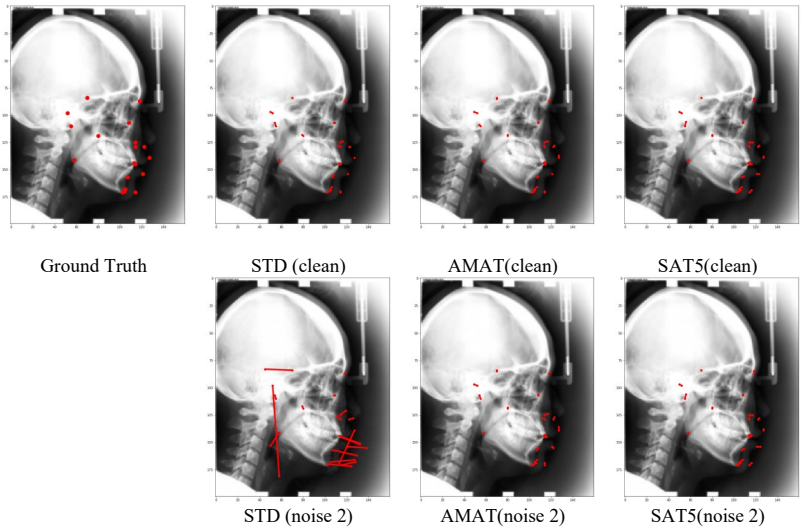


Figure 3: Examples of adversarial attacks against cephalometric landmark detection (L2 norm). The red lines indicates the distance between ground truths and predicted locations

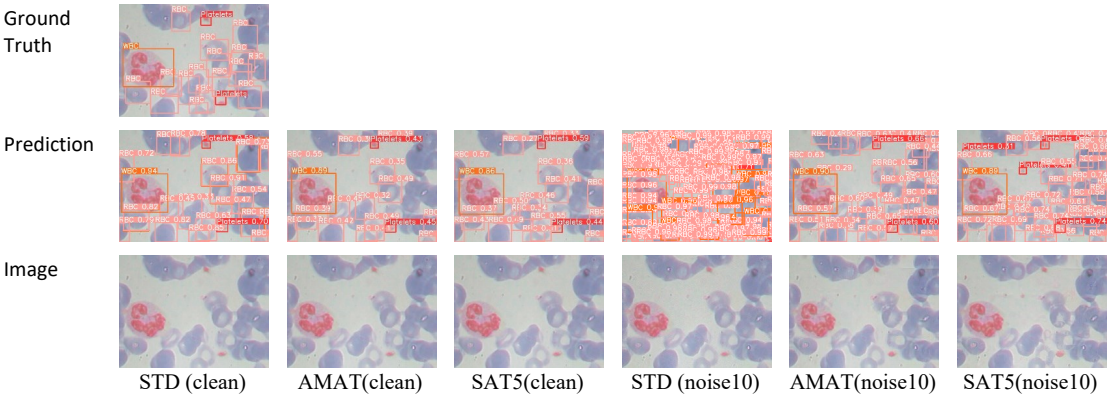


Figure 4: Examples of adversarial attacks against blood cell detection (L2 norm)